Polarization Measurement Using Vortex Beams With Non-Integer Orbital Angular Momentum

Aning Ma , Zhongqiang Zhang , Yurong Wang, Di Geng, Xinyi Tian, and Haofeng Huang

Abstract—**Polarization measurement has been used for many optical applications in science and technology. Herein, we adopt a reliable method to measure the polarization parameters of incident light, including principal axis, chirality and ellipticity based on the superposition of two orthogonal vortex beams with non-integer topological charges (TCs). All three polarization parameters can be measured and analyzed by the interference pattern produced by the superposition of two vortex beams with $\ell_1 = 1$ and $\ell_2 = 0.5$. The relationship between the principal axis of polarization and the interference pattern is deduced theoretically. The measurement results agree with the theoretical formulation very well. The advantages of simplicity make this method have a good application prospect in polarization measurement, optical communication, micro-particles manipulation and quantum science.**

Index Terms—**Polarimetry, nano-photonics, vortex beams.**

I. INTRODUCTION

POLARIZATION, as one of the fundamental properties of light, is defined as the direction in which electromagnetic radiation oscillates. Polarization has widely expanded the applications of astronomy [1], remote sensing [2], biology [3], medicine [4], [5] and microscopy [6]. According to the polarization information, one can acquire more valuable information about the environment, such as tissue properties and texture of reflecting surfaces, the optical activity of different materials, or the orientation of light emitters. The polarization of light differs from other properties of light such as amplitude and frequency because of its vectorial peculiarity, which adds to the complexity of polarimetry [2]–[7]. As we all know, vortex beams described by spatial helical phase wavefront can carry quantized orbital angular momentum (OAM). Due to various distinguishable characteristics, vortex beams with a helical phase structure described by $\exp(i\ell\theta)$ have been widely explored in classic optics [8], nonlinear optics [9], information coding [10]–[13], optical communication [14], quantum optics [15], microparticle manipulation [16], [17]. Recently, radial opening in intensity profile of non-integer order OAM beams is further explored.

Some fascinating applications of non-integer OAM have been reported, for instance, high dimensional quantum entanglement of two photons [18] and microparticles transportation guiding [19]. However, polarization measurement based on non-integer OAM superposition has not been explored so far.

In this paper, we propose a method based on the superposition of two orthogonal circular polarization states carrying ono-integer OAM beams with different TCs to realize the polarization measurement of incident light. An arbitrary polarization can be derived from elliptic polarization and determined by three parameters: principal axis, ellipticity, and chirality [20]. Here, the principal axis of polarized light can be understood as the angle between the major axis of the ellipse and the *x*-axis. Chirality can be interpreted as the direction in which vibrations rotate (clockwise or counterclockwise), while the ellipticity η is described by the ratio of the intensity of its left-handed circular polarization (LCP) and right-handed circular polarization (RCP) components. All three polarization characteristics of incident light can be measured and analyzed by the interference pattern produced by the superposition of two OAM beams with $\ell_1 = 1$ and $\ell_2 = 0.5$.

II. THEORY

The general Laguerre-Gaussian (LG) modes have *p* radial nodes in its amplitude. We will limit ourselves to singly-ringed modes with $p = 0$. The electric field distribution of the LG beam with helical phase structure is described as [21]

$$LG_p^\ell = A \cdot \exp\left[\frac{-ikr^2z}{2\left(z_R^2 + z^2\right)}\right] \exp\left[-i\phi\left(\ell\right)\right] \exp\left(i\ell\theta\right) \quad (1)$$

where θ is the azimuth angle, ℓ is the TCs of the helical phase term.

$$A = \sqrt{\frac{2}{\pi\left|\ell\right|}} \frac{1}{w\left(z\right)} \left[\frac{\sqrt{2}r}{w\left(z\right)}\right]^{|\ell|} \exp\left[\frac{-r^2}{w(z)^2}\right] L_p^{|\ell|}\left[\frac{2r^2}{w(z)^2}\right] \quad (2)$$

In Eq. (2), $w(z) = w_0\sqrt{2 + z^2/z_R^2}$ represents the radius of LG beam, $k = 2\pi/\lambda$ represents wave number, $z_R = kw_0^2/2$ represents the Rayleigh distance, $\phi(\ell) = (2p + |\ell| + 1)\tan^{-1}(z/z_R)$ represents the Gouy phase. The intensity distribution of the LG beam with a helical phase structure is similar to a doughnut shape due to the phase singularity at the central of the beam. In the intensity profile of the LG beam, the distance between the center spot and the maximum intensity spot is described as $Z = w(z)\sqrt{|\ell|/2}$, which determines the radius of the LG intensity profile.

Considering now the superposition of two collinear component LG beams with topological charges ℓ_1 and ℓ_2, the composite beam can be expressed as

$$E_C = E_L \cdot LG^{\ell_1} \cdot e^{iv_L} + E_R \cdot LG^{\ell_2} \cdot e^{iv_R} \quad (3)$$

where E_L, E_R represent the amplitudes of two component beams, respectively. $\Delta v = v_L - v_R$ denotes the phase difference between two component beams. The composite beam can be characterized by passing through an Analyzer (linear polarizer) whose transmission axis forms an angle γ with respect to the x direction. The combined intensity of two LG beams is

$$I = |E_C|^2 = 2E^2 \left\{ 1 + \cos \left[(\ell_1 - \ell_2) \left(\theta + \frac{\Delta v + \gamma}{\ell_1 - \ell_2} \right) \right] \right\} \quad (4)$$

It can be obtained that the light intensity reaches its maximum at $\Delta v = (\ell_1 - \ell_2)\theta_{\max} + n\pi$, when the transmission axis of the linear Analyzer is all consistent with x-axis ($\gamma = 0$). When $\ell_1 = 1$ and $\ell_2 = 0.5$, combined with $\psi = \Delta v/2$ the angle between the principal axis and x-axis is

$$\psi = \frac{1}{4}\theta_{\max} \quad (5)$$

When two LG beams are superimposed collinearly, they will produce an interference pattern that depends on the relative amplitude and the phase of component beams. Any polarization state can be viewed as a linear superposition of orthogonal components with different amplitudes or phases. Therefore, by detecting the phase difference and amplitude ratio between the two components, the polarization state of the beam can be determined. In MATLAB simulation, we can adjust the phase difference and amplitude ratio of two orthogonal LG beams by changing α and β. The angles of the transmission axis of linear polarizer and the fast axis of quarter wave plate (QWP) with respect to the x-axis are denoted as α and β, respectively. The Jones vector of the linearly polarized light and Jones matrix of the QWP are $\begin{pmatrix} \cos \alpha \\ \sin \alpha \end{pmatrix}$ and $e^{-i\pi/4} \begin{pmatrix} \cos^2\beta + i\sin^2\beta & (1-i)\sin\beta\cos\beta \\ (1-i)\sin\beta\cos\beta & \sin^2\beta + i\cos^2\beta \end{pmatrix}$, respectively. The Jones vector of the light beam emitted by the laser after passing through the linear polarizer and the QWP is governed by the following relation.

$$\Psi = e^{-i\pi/4} \begin{pmatrix} \cos^2\beta + i\sin^2\beta & (1-i)\sin\beta\cos\beta \\ (1-i)\sin\beta\cos\beta & \sin^2\beta + i\cos^2\beta \end{pmatrix} \begin{pmatrix} \cos \alpha \\ \sin \alpha \end{pmatrix}$$

$$= \frac{a}{\sqrt{2}} \begin{bmatrix} 1 \\ -i \end{bmatrix} + \frac{b}{\sqrt{2}} \begin{bmatrix} 1 \\ i \end{bmatrix} \quad (6)$$

Here, the components of RCP and LCP are represented by a and b respectively. By rotating α and β in simulation, different interference patterns appear, which can be used to measure the polarization state of light. It should be mentioned that the interference patterns generated by the superposition of fractional vortex beams also have some wonderful properties in the derivation of the principal axis of incident light. These properties cannot be simply described by Eq. (5). However, there are still rules to be found, and we will give our own thinking in the subsequent simulations. In addition to the principal axis of polarization, chirality and ellipticity can also be determined by
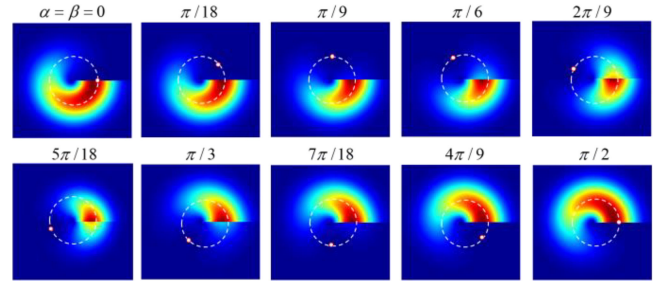

Fig. 1. $\alpha = \beta > 0$ corresponding interference pattern.

the interference pattern. In our method, the chirality of polarized light can be measured by the pixel distance between the center spot and the maximum intensity spot along the split line in the interference pattern. The calculation of the ellipticity of polarized light can also be implemented by the ratio between the minimum and maximum intensity of the intensity distribution along the circle (the radius is the distance between the center spot and the minimum intensity spot on the split line) in the interference pattern. An arbitrary polarization state can be described by three polarization parameters including the principal axis of polarization, the chirality and ellipticity. Therefore, we come up with a new way to measure three polarization parameters of incident light based on the intensity profile generated by the superposition of two LG beams with $\ell_1 = 1$ and $\ell_2 = 0.5$.

III. RESULTS AND DISCUSSIONS

The principal axis of polarization on the interference pattern generated by the superposition of two LG modes with TCs of $\ell_1 = 1$ and $\ell_2 = 0.5$ is initially investigated. Fig. 1 shows the simulated intensity profile based on the superpositions of OAM states with $\ell_1 = 1$ and $\ell_2 = 0.5$ under illumination of a linearly polarized (LP) beams. It is not difficult to find that the intensity profile of the composite beam has radial dislocations in the horizontal direction. When $\alpha = \beta = 0$, there is an intensity lobe similar to a "crescent" in the interference pattern. With the increasing of α, the intensity lobes rotate counterclockwise. When the intensity lobes pass through radial dislocations in the horizontal direction, the intensity gradually disappears and the range of the intensity lobes gradually decreases. When α continues to increase, the light intensity reappears above the radial dislocation, and the range of the intensity lobes gradually increases. Different from the interference patterns produced by the superposition of integer-order OAM beams [20], the radial dislocations in fractional-order beams make the variation of intensity lobes discontinuous, so that it is difficult to predict the principal axis according to the changes of intensity lobes. However, when $\alpha = \beta > 0$, there is a peripheral vortex (zero intensity point) around the intensity lobe, and as α and β increase, the peripheral vortex which are denoted by a white dot rotates counterclockwise on a white dashed circle, as shown in Fig. 1. It should be mentioned that the principal axis of incident light can be uniquely determined by setting $\alpha = \beta$ in MATLAB simulation. Therefore, when the principal axis of incident light is
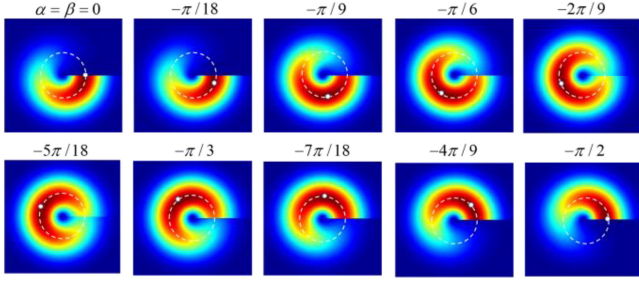
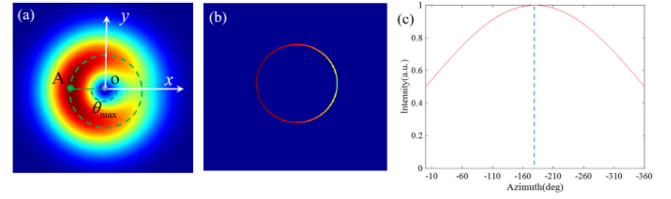Fig. 2. $\alpha = \beta < 0$ corresponding interference pattern.

Fig. 3. Measurement of the principal axis of incident light. (a) The intensity profile generated by the superposition of two OAM states with TCs $\ell_1 = 1$ and $\ell_2 = 0.5$ where the incident light is LP and its principal axis is $-\pi/4$ relative to the *x*-axis. The size of the image is 600×600 pixels. (b) The intensity profile corresponding to the green circle. (c) The relation between the azimuth angle and its corresponding strength.

in the first and third quadrant ($\alpha = \beta > 0$), it can be determined according to the peripheral vortex (zero intensity point) in the interference pattern.

In addition, Fig. 2 shows the case of $\alpha = \beta < 0$, the same as the case $\alpha = \beta > 0$, the interference pattern also has radial dislocations in the horizontal direction, and the intensity lobes are initially in the radial direction. As α continues to decrease, the intensity lobes in the interference pattern rotate clockwise, and the range of the intensity lobes resembling the "crescent" gradually increases. When $\alpha = \beta = -\pi/4$, the range of the intensity lobes reaches the maximum, and the upper and lower parts of the radial dislocation have the same range. As α continues to decrease, the extent of the intensity lobes gradually decreases from the lower part of the radial dislocation. Below the dislocation, the intensity is masked when passing through the radial dislocation. When $\alpha = \beta = -\pi/2$, the intensity lobes regain their crescent-like shape and are above the radial dislocations. The azimuth corresponding to the maximum intensity point of the lobe undergoes a continuous change from 0 to -2π. It should be mentioned that when α continues to decrease, the intensity distribution reappears below the radial dislocation, and gradually decreases above, similar to the case of $\alpha = \beta > 0$, thus forming a cycle. Therefore, when the principal axis of incident light is in the second and fourth quadrants ($\alpha = \beta < 0$), the principal axis of incident light can be determined according to the azimuth angle corresponding to the maximum intensity point which is denoted by a white dot rotating clockwise on a white dashed circle in the interference pattern, as shown in Fig. 2.

To sum up, the principal axis of incident light is determined by the azimuth angle corresponding to the peripheral vortex (minimum intensity point inside the region) or the maximum intensity point of intensity lobe in the interference pattern. Eq. (5) can be further formulated as

$$\psi = \frac{1}{4}\theta_{\mathrm{max/min}} \qquad (7)$$

where $\theta_{\mathrm{max/min}}$ represents the azimuth angle corresponding to the maximum intensity point of intensity lobes in the interference pattern or the peripheral vortex (the minimum intensity point of the image). It is worth noting that the maximum intensity point of intensity lobe and the peripheral vortex do not appear at the same time. When $\alpha = \beta = 0, \pm\pi/2$, the maximum intensity points of intensity lobes and the peripheral vortices are

merged together, so according to any one of them, the principal axis of incident light can be determined.

In order to verify the above speculation, the interference superposition of LP light is simulated in MATLAB, as shown in Fig. 3. Fig. 3(a) shows the interference pattern corresponding to the LP light whose principal axis is $-\pi/4$. The intensity maximum point of the intensity lobes in the pattern is represented by A, and a circle is drawn with the distance from the center point O to point A as the radius. The intensity distribution along the green dotted circle is extracted, as shown in Fig. 3(b). It is easy to know from the above analysis that when α and β take negative values, the intensity lobes rotate clockwise, so the azimuth angle corresponding to the maximum intensity also rotates clockwise. In order to have a more accurate correspondence between the intensity and azimuth on the circle, the distribution of the intensity ring along the clockwise direction is shown in Fig. 3(c). The blue dotted line points to the point of maximum intensity, and the corresponding azimuth angle $\theta_{\max} = -\pi$ satisfies Eq. (13), which preliminarily verifies the effectiveness of the method.

To further illustrate that this measurement method can be applied to an incident light with any polarization principal axis, Fig. 4(a) shows the interference patterns corresponding to LP light with different principal axes $(0, -\pi/6, \pi/4$ and $\pi/3)$. Here, the interference patterns corresponding to different principal axes are processed according to the measurement methods described in Fig. 3. Take the center point O as the center of the circle and the distance from point O to the maximum intensity point as the radius to make a circle, and extract the intensity along the green dotted circle, as shown in Fig. 4(b). Considering that the main axis is in the first and third or second and fourth quadrants, the interference pattern will rotate counterclockwise or clockwise. Therefore, take out the corresponding normalized intensity counterclockwise or clockwise along the azimuth angle on the intensity ring, as shown in Fig. 4(c). Among them, when the main axis is positive, the blue dotted line points to the minimum intensity point, and when the main axis is negative, the blue dotted line points to the maximum intensity point, and the corresponding azimuth angles all satisfy the Eq. (9). The results show that the simulation results are in good agreement with the theoretical analysis, and the simulation of multiple sets of results fully verifies the effectiveness of the method for measuring the principal axis of polarization.
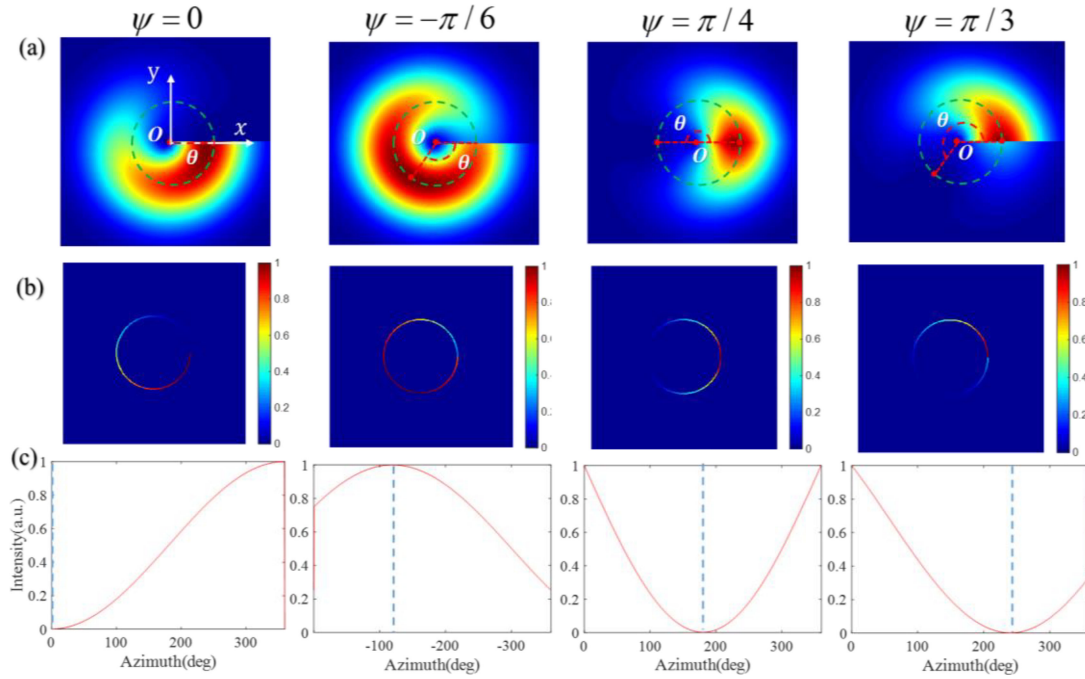
Fig. 4. Measurement of the principal axis of the incident light with different principal axes. (a) The numerical simulation results when the principal direction of the incident light are $0, -\pi/6, \pi/4$ and $\pi/3$, respectively. (b) The intensity distribution based on the green circle. (c) The relationship between azimuth and intensity along the circle.
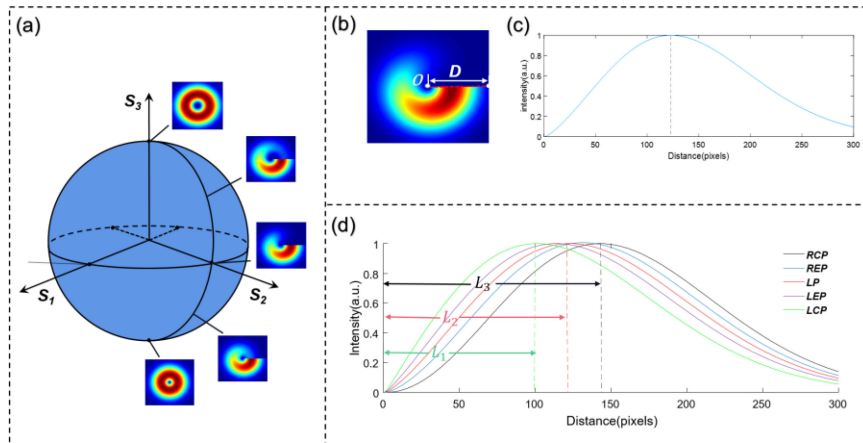

Fig. 5. Measurement of the chirality of incident light. (a) The intensity profile generated by superposition is displayed on the Poincare sphere, which corresponds to RCP, REP, LP, LEP, and LCP from top to bottom. The principal axes of these polarization states are all consistent with x-axis. (b) The intensity profile of the interference pattern generated by a LP light. (c) The intensity distribution corresponding to the red dotted line in (b) varying with pixel distance D. (d) The intensity distribution along the red dotted line varying with pixel distance D under five different polarized states of light.

The chirality of polarized light can be distinguished by the interference pattern as well. Fig. 5(a) illustrates the simulated interference pattern of five different polarization states displayed on the Poincaré sphere, which are RCP, REP (right-handed elliptical polarization), LP, LEP (left-handed elliptical polarization) and LCP from top to bottom. In the simulation, we can rotate α while keeping β constant to achieve a superposition of two components with different amplitudes. Take the interference pattern shown in Fig. 5(b) as an example ($\alpha = 0, \beta = 0$), the feasibility of distinguishing chirality by interference patterns

is discussed. Here, $D = 300$ pixels is the distance between the center point O and the edge of the image. The normalized intensity distribution along the dash line D is extracted, as shown in Fig. 5(c). The chirality of polarized light can be distinguished by the distance between the center point O and the pixel whose light intensity reaches its maximum along the dash line. Fig. 5(d) shows the relation between the normalized intensity on the dash line and pixels when the incident light with different polarization states (RCP, REP, LP, LEP, LCP) is illuminated. The distance L_1, L_2, L_3 corresponds to the distance between the center point
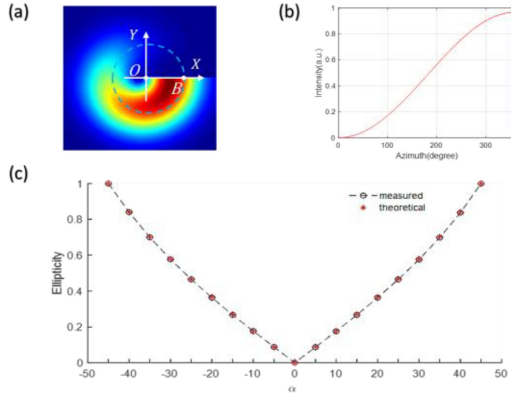
Fig. 6. Measurement of the ellipticity of incident light. (a) The interference pattern generated by LP light along the *x*-axis. (b) The distribution of the normalized intensity along the blue circle as a function of azimuth angle. (c) The comparison between the measured ellipticity and the theoretical value under different polarization states of light.
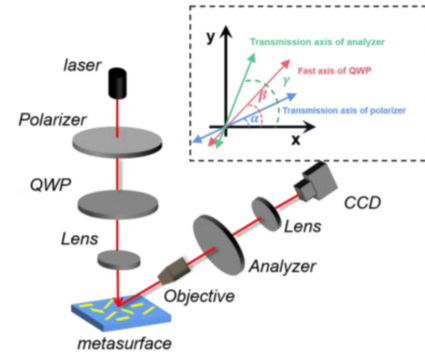

Fig. 7. Schematic diagram of experimental setup. The polarization state of the incident light can be implemented by a linear polarizer and a QWP. After passing through the linear analyzer, the intensity profile of the composite beam generated by the metasurface is recorded by the CCD camera. The linear polarizer, QWP, and analyzer's rotation angle with respect to the *x*-axis are denoted by α, β, γ, respectively.

O and the maximum intensity point at LCP, LP, RCP, respectively. When the light illuminates with an unknown polarization state, the pixel distance L_3 is greater than L_2, which reflects that the chirality of the incident light is right-handed. In addition, the pixel distance L_1 is smaller than L_2, which reflects that the chirality of the incident light is left-handed. In fact, we can also distinguish the ellipticity of the incident light rather than just the chirality according to the distance *L*. However, this approach can't give an accurate ellipticity value. Therefore, we propose a more effective method to accurately calculate the ellipticity of polarized light.

In order to accurately calculate the ellipticity of polarized light, the interference pattern is generated by LP light along the *x*-axis, as shown in Fig. 6(a). The radius of the blue circle in the intensity profile is the distance between the center spot O and the minimum intensity spot B on the *x*-axis. Similar to measuring the principal axis, the normalized intensity distribution along the circle as a function of azimuth angle is shown in Fig. 6(b). The ellipticity η of polarized light can be calculated by the ratio of minimum intensity and the maximum intensity on the blue circle, that is $\eta = \sqrt{I_{\min}/I_{\max}}$. Different ellipticity of the incident light are obtained by rotating angle $\alpha = -45°, -40°, -30°, -20°, -10°, 0°, 10°, 20°, 30°, 40°, 45°$ while maintaining angle β and γ are fixed along *x*-axis. According to $\eta = \sqrt{I_{\min}/I_{\max}}$, the ellipticity of polarized light is calculated, as shown in Fig. 6(c). $\eta = 0$ and $\eta = 1$ correspond to LP and CP, respectively. The measured and theoretical ellipticity values of light with different polarization states agree very well with each other. This approach provides a fast and accurate way to measure the ellipticity of the incident light based on the interference pattern generated by superposition of two OAM beams with $\ell_1 = 1$ and $\ell_2 = 0.5$.

In order to explain the engineering application background of this paper more clearly, the schematic of follow-up experimental setup is shown in Fig. 7. A metasurface should be designed and fabricated to generate a composite beam based on the superposition of two orthogonal vortex beams with non-integer topological charges. The wavelength of the laser is set at 650 nm.

The linear polarizer and QWP are used to generate an arbitrary polarization light. A lens focuses the beam completely on the metasurface. An objective lens amplifies the composite beam. After passing through the linear analyzer, the intensity profile of the composite beam generated by the metasurface is recorded by the CCD camera. The angles of the transmission axis of linear polarizer and the fast axis of QWP with respect to the *x*-axis are denoted as α and β, respectively. The angle between the transmission axis of the linear analyzer and the *x*-axis is γ, as shown in the inset of Fig. 7.

IV. CONCLUSION

A simple polarization measurement is proposed based on superposition of two OAM beams with non-integer TCs $\ell_1 = 1$ and $\ell_2 = 0.5$. The polarization parameters including principal axis, chirality and ellipticity are measured by the interference pattern. Moreover, the simulated results have been validated by the theoretical formula and results, and good agreements are achieved, which verifies the effectiveness of this polarization measurement. This work will be of great importance for practical applications of OAM devices and polarization detection.

REFERENCES

[1] F. Lei, A. J. Dean, and G. L. Hills, "Compton polarimetry in gamma-ray astronomy," *Space Sci. Rev.,* vol. 82, no. 3, pp. 309–388, 1997.

[2] J. S. Tyo, D. L. Goldstein, D. B. Chenault, and J. A. Shaw, "Review of passive imaging polarimetry for remote sensing applications," *Appl. Opt.,* vol. 45, no. 22, pp. 5453–5469, 2006.

[3] J. Bailey *et al.*, "Circular polarization in Star- Formation regions: Implications for biomolecular homochirality," *Science,* vol. 281, no. 5377, pp. 672–674, 1998.

[4] T. Šmidlehner, M. Badovinac, and I. Piantanida, "Pyrene–cyanine conjugates as multipurpose fluorescent probes for non-covalent recognition of ds-DNA, RNA and proteins," *New J. Chem.,* vol. 42, no. 9, pp. 6655–6663, 2018, doi: 10.1039/C8NJ00055G.

[5] N. Ghosh and A. Vitkin, "Tissue polarimetry: Concepts, challenges, applications, and outlook," *J. Biomed. Opt.,* vol. 16, no. 11, 2011, Art. no. 110801.

[6] Y. Wang *et al.*, "Differentiating characteristic microstructural features of cancerous tissues using Mueller matrix microscope," *Micron,* vol. 79, pp. 8–15, 2015.

[7] F. Yue *et al.*, "Highly sensitive polarization rotation measurement through a high-order vector beam generated by a metasurface," *Adv. Mater. Technol.,* vol. 5, no. 5, 2020, Art. no. 1901008.

[8] Y. Wang *et al.*, "Integrated photonic emitter with a wide switching range of orbital angular momentum modes," *Sci. Rep.,* vol. 6, no. 1, 2016, Art. no. 22512.

[9] K. Dholakia, N. B. Simpson, M. J. Padgett, and L. Allen, "Second-harmonic generation and the orbital angular momentum of light," *Phys. Rev. A,* vol. 54, no. 5, pp. R3742–R3745, 1996.

[10] J. Leach, M. J. Padgett, S. M. Barnett, S. Franke-Arnold, and J. Courtial, "Measuring the orbital angular momentum of a single photon," *Phys. Rev. Lett.,* vol. 88, no. 25, 2002, Art. no. 257901.

[11] G. C. G. Berkhout and M. W. Beijersbergen, "Method for probing the orbital angular momentum of optical vortices in electromagnetic waves from astronomical objects," *Phys. Rev. Lett.,* vol. 101, no. 10, 2008, Art. no. 100801.

[12] G. Gibson *et al.*, "Free-space information transfer using light beams carrying orbital angular momentum," *Opt. Exp.,* vol. 12, no. 22, pp. 5448–5456, 2004.

[13] B. Thidé *et al.*, "Utilization of photon orbital angular momentum in the low-frequency radio domain," *Phys. Rev. Lett.,* vol. 99, no. 8, 2007, Art. no. 087701.

[14] T. Šmidlehner, I. Piantanida, and G. Pescitelli, "Polarization spectroscopy methods in the determination of interactions of small molecules with nucleic acids – tutorial," *Beilstein J. Org. Chem.,* vol. 14, pp. 84–105, 2018.

[15] L. Marrucci *et al.*, "Spin-to-orbital conversion of the angular momentum of light and its classical and quantum applications," *J. Opt.,* vol. 13, no. 6, 2011, Art. no. 064001.

[16] Y. Wang *et al.*, "Generating optical superimposed vortex beam with tunable orbital angular momentum using integrated devices," *Sci. Rep.,* vol. 5, no. 1, 2015, Art. no. 10958.

[17] A. Jesacher, S. Fürhapter, S. Bernet, and M. Ritsch-Marte, "Size selective trapping with optical 'cogwheel' tweezers," *Opt. Exp.,* vol. 12, no. 17, pp. 4129–4135 2004.

[18] S. H. Tao, X. C. Yuan, J. Lin, X. Peng, and H. B. Niu, "Fractional optical vortex beam induced rotation of particles," *Opt Exp.,* vol. 13, no. 20, pp. 7726–7731, 2005.

[19] S. S. R. Oemrawsingh *et al.*, "Experimental demonstration of fractional orbital angular momentum entanglement of two photons," *Phys. Rev. Lett.,* vol. 95, no. 24, 2005, Art. no. 240501.

[20] A. Ma, Y. Intaravanne, J. Han, R. Wang, and X. Chen, "Polarization detection using light's orbital angular momentum," *Adv. Opt. Mater.,* vol. 8, no. 18, 2020, Art. no. 2000484.

[21] L. Allen, M. W. Beijersbergen, R. J. C. Spreeuw, and J. P. Woerdman, "Orbital angular momentum of light and the transformation of Laguerre-Gaussian laser modes," *Phys. Rev. A,* vol. 45, no. 11, pp. 8185–8189, 1992.